# Efficient laser-plasma acceleration of protons via near-critical mass limited targets

Johannes Gebhard, 1,\* Peter Hilz, 3,4 Felix Balling, 1 Joey Kalis, 1 Martin Speicher, Leonard Doyle, 1 Alexander Sävert, 3,2,4 Georg Schäfer, 3,4 Pooyan Khademi, 3,4 Bin Liu, 3,4 Matt Zepf, 2,3,4 and Jörg Schreiber, 1,7 <sup>1</sup>Fakultät für Physik, Ludwig-Maximilians-Universität München, Am Coulombwall 1, Garching 85748, Germany <sup>2</sup>Institut für Optik und Quantenelektronik, Max-Wien-Platz 1, Jena 07743, Germany <sup>3</sup>Helmholtz-Institut Jena, Fröbelstieg 3, Jena 07743, Germany <sup>4</sup>GSI Helmholtzzentrum für Schwerionenforschung GmbH, Planckstraße 1, Darmstadt 64291, Germany

(Received 28 August 2024; revised 22 April 2025; accepted 1 July 2025; published 9 September 2025)

Isolated micro-targets are a promising avenue to high-performance laser-driven proton and ion accelerators due to their ability to confine the coupled laser energy to a small volume and small number of particles. Experimental results on proton emission from levitated plastic micro-spheres with an initial diameter of 1 µm are presented. For a laser with only 0.4 J contained within the central spot, proton energies of up to 27 MeV were observed with micro-spheres pre-expanded to near-critical density. Three-dimensional PIC simulations reveal that the combination of a ponderomotively driven process similar to radiation pressure 'hole-boring' generates a dense plasma bunch propagating at 0.1 c with the subsequent expansion of the moving bunch driven by hot electrons boosting the maximum proton energy E<sub>max</sub> considerably. Simulations agree well with the observed experimental results and suggest a scaling of 54 MeV/J<sup>1/2</sup>, predicting that 100 MeV protons are possible with only 4 J in a Gaussian spot.

DOI: 10.1103/z7y1-1zbz

#### I. INTRODUCTION

The majority of experiments on laser-plasma acceleration of ions relies on planar targets or targets with a transverse extent significantly exceeding the width of the tight laser focus. Through optimization of the laser and target parameters, through suppression of pre-pulses and reducing the thickness, proton energies have increased from 60 MeV [1] to 160 MeV [2] over the past two decades. Although there are a number of distinct acceleration mechanisms [3], they generate quasistatic fields of order 10 s of MeV/µm by charge separation between laser accelerated electrons and the ion background. Prominent mechanisms with rather clear definition are target normal sheath acceleration [4] for opaque (overdense) targets, radiation pressure [5], and magnetic vortex acceleration [6] for transparent (underdense) targets. For targets with a lateral extend smaller or comparable to the laser wavelength, ion acceleration is a result of the combined action of relativistically induced transparency [7–11], the radiation pressure-based processes hole-boring [5,12,13] and the related shock acceleration [14,15], laser-piston [16], radiation pressure [17,18], or light-sail [19,20] acceleration.

Disentangling the various contribution has remained challenging in experiments with planar targets, due to the radial and temporal distribution of laser intensity spanning over

Published by the American Physical Society under the terms of the Creative Commons Attribution 4.0 International license. Further distribution of this work must maintain attribution to the author(s) and the published article's title, journal citation, and DOI.

many orders of magnitudes, which results in the intra-pulse variation electron density during the laser pulse. Therefore, the observed kinetic energy distribution of emitted ions is typically broad and extends to a cut-off energy. The laser pulse energy poses ultimate limits to achievable ion energies [21] and a heuristic observation of published results yields a scaling slightly weaker than the square root scaling expected from the ponderomotive electron energy scaling at  $E_{\text{max}} = 7.3E_L^{0.4}$ [22,23] or over 30 J on target to reach 30 MeV protons. For acceleration mechanisms driven by laser-accelerated electrons, the transport of relativistic electrons through the target has long been understood to be a limiting factor in the conversion of laser energy to ion kinetic energy, with mass-limited targets being discussed as a means to enhance coupling to the protons.

Of particular interest for optimizing the acceleration are targets with electron densities of order of the relativistic critical electron density  $n_c$ , which is at the transition where a laser pulse with central frequency  $\omega_L$  and normalized amplitude of the laser vector potential  $a_L$  is resonant with the plasma frequency  $\omega_p/\gamma$ , with  $\gamma \approx (1 + a_L^2/2)^{(1/2)}$  as the average Lorentz factor of electrons. Studying this regime experimentally has remained difficult, because for high-intensity NIR lasers,  $n_c$  is of order  $a_L/100$  of solid density or 100  $a_L$  times the density of an ideal gas at standard conditions. The most common approach, therefore, relies on pre-expanding solid or nanostructured foils. Their transverse dimension is larger than the laser focal spot though and this again leads to a mixture of acceleration processes that are difficult to disentangle. Nearcritical targets with dimensions smaller than the laser focal spot are, therefore, also a natural choice to simplify matters and have hence been studied using particle in cell simulations [24–27]. In these simulations, laser pulses are typically

<sup>\*</sup>Contact author: johannes.gebhard@physik.uni-muenchen.de

<sup>†</sup>Contact author: joerg.schreiber@lmu.de

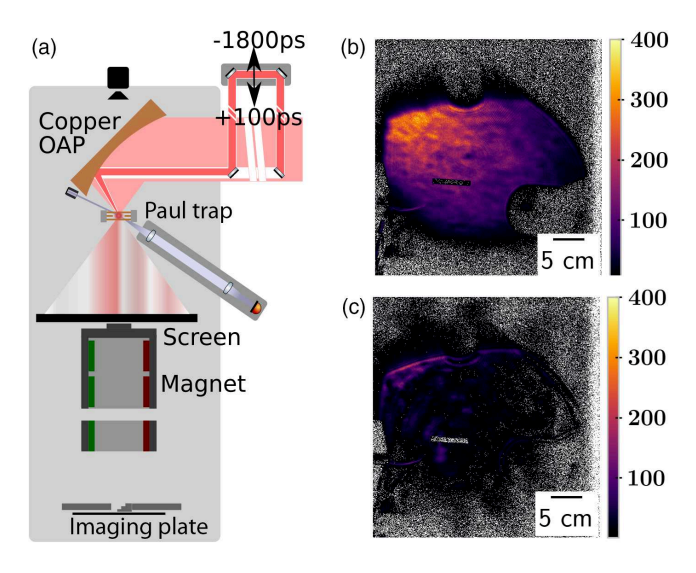


FIG. 1. (a) Schematic experimental setup showing pre-pulse pick-off, delay stage, focusing optics, Paul-trap for positioning levitating microsphere targets, scatter screen for recording laser beam profiles, and magnetic spectrometer for measuring the proton energy distributions. (b) Reference laser beam profile recorded without target (distorted by pre-pulse mirror clipping and OAP projection). (c) Laser beam profile for the shot yielding the highest maximum proton energy.

modeled as ideal Gaussian pulses which contain less energy than realistic pulses and we refer to this energy as effective laser energy.

While simulating isolated targets is straightforward, experimentally such isolated micro-plasmas are highly challenging. They can be provided by a Paul-trap-based target system that we have developed [28]. This system enables positioning of plastic spheres with diameters as small as 0.5  $\mu$ m and was used for ion acceleration experiments at long-pulse Petawatt (PW) laser systems (150 fs, 500 fs) [29,30]. Experiments with 500 fs laser pulses focused onto spheres with a diameter of 1  $\mu$ m yielded directed proton bunches with energies between 20 and 40 MeV [30], and the efficient acceleration was limited to a period of  $\sim$ 10 s of fs during which the density of the expanding plasma matched.

### II. EXPERIMENTAL SETUP

Here, we present the first results of experiments with such isolated targets under conditions where the pulse duration is matched to the natural expansion timescale and with temporal contrast which enables an active pre-expansion of the target prior to the main pulse irradiation, rather than relying on an intra pulse expansion. We observe a optimum, i.e., maximum proton fluence and energy, when the target's electron density is relativistically critical. Three-dimensional particle-in-cell simulations can reproduce the experimental results and reveal insight into the underlying acceleration process, while predicting the possibility of generating intense proton beams with energies well beyond 100 MeV with laser pulses containing as little as 4 J of effective energy.

Figure 1(a) shows core experimental setup. We applied a linear Paul-trap with an active stabilization to position the

levitated particle (0.5 µm radius plastic spheres) in the focus of the laser pulse. A pre-pulse with peak intensity between  $10^{15}$  and  $10^{16}$  W/cm² was used to actively trigger a controlled plasma expansion of the plastic sphere 0–1800 ps prior to the arrival of the main pulse. The JETi laser (22 fs Ti: Sapphire pulses at  $\lambda = 800$  nm) energy was reduced to 1.4 J by the plasma mirror setup used to enhance the contrast of the main pulse and obscuration by the pre-pulse assembly. The peak intensity was calculated to be  $6 \times 10^{20}$  W/cm² based on the measured laser parameters and high dynamic range focal spot image with 5 orders of magnitude dynamic range. While the smallest full width at half maximum spot diameter focal spot was 1.6 µm, alignment uncertainties resulted in variation of the spot size and, therefore, the peak intensity.

For extended and planar targets, the full laser energy interacts with the target with a wide range of intensities and significant energy outside the main focal spot. In the case of a target that is small compared to the laser focus, the energy outside the main spot does not contribute to the interaction. For the interpretation of the data and using appropriate laser conditions in the simulations, we matched a Gaussian spot distribution to the experimental focus with the same diameter and the same peak energy. This *matched spot* contained 0.4 J of *effective energy* and this was used as input for simulations. <sup>1</sup>

The accelerated protons were registered by an image plate detector behind a magnetic dipole spectrometer with a horizontal entrance slit (for further details see Appendix), which allowed the maximum proton energy  $E_m$  and the angular proton fluence  $dN/d\Omega$  above the 2.6 MeV detection threshold to be determined. The levitated sphere was trapped in a Paul trap [28]. Ambient vibrations resulted in a residual oscillation amplitude of the levitated sphere (~2 μm amplitude) and a laser-pointing jitter ( $\sim$ 2 µm amplitude) causing shot-to-shot fluctuations of the recorded spectra. We were, therefore, limited to 23 data shots without pre-pulse and 71 shots with pre-pulse at various delays. The fluctuation in the coupling to the levitated sphere was determined by measuring the transmitted laser light on a scatter screen for each shot. Examples of the scatter screen data are shown in Figs. 1(b) and 1(c). The transmission T was calculated for every shot by dividing the transmitted integrated intensity as shown in Fig. 1(c) by the reference image taken without a target [Fig. 1(b)]. The laser energy loss L = 1 – T is related to the radial extent  $r_c$ of the plasma, where the density exceeds the critical density at the time of interaction of the main pulse (see Appendix for details). Using this approach, we assigned a value  $r_c$  to each shot with the ratio  $r_c/r_0$  serving as an ordering parameter to sort our data according to comparable interaction conditions in each shot.

Assuming that the change in transmission for different ordering parameters  $r_c/r_0$  is due to pre-expansion, we can determine the interaction conditions. Based on the initial electron density of a fully ionized, nonexpanded polystyrene sphere of  $195n_c$  for our laser wavelength and assuming a spherically symmetric pre-expansion induced by the prepulse

<sup>&</sup>lt;sup>1</sup>The low effective energy compared to the pulse energy was primarily due to aberrations and surface roughness of the diamond-turned-parabola.

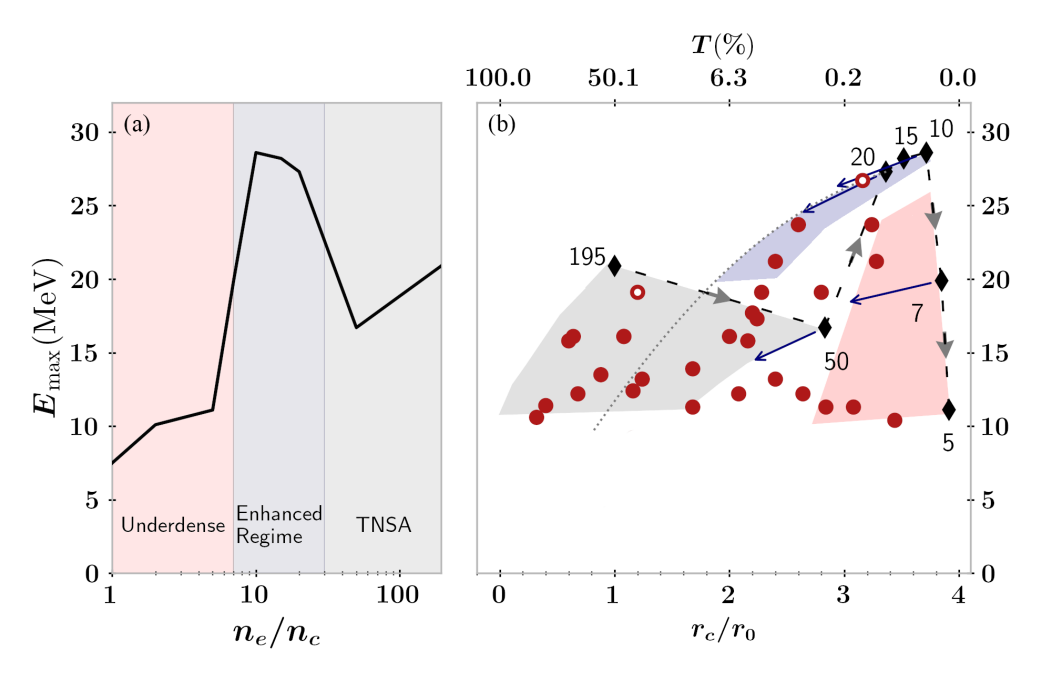


FIG. 2. (a)  $E_{\text{max}}$  from PIC simulations for spheres of constant mass vs peak density  $n_0/n_c = 5, 7, 10, 15, 20, 50$ , and 195 with regimes indicated. (b)  $E_{\text{max}}$  from simulation and  $E_{\text{max}} > 10 \,\text{MeV}$  from measurements vs ordering parameter  $r_c/r_0$  (calculated from laser transmission T) as experimental proxy for peak electron density  $n_0$ . Arrows show the effect on  $E_{\text{max}}$  and  $r_c/r_0$  when displacing the target by 1  $\mu$ m in simulations, for larger displacement the example  $n_0/n_c = 20$  follows the dotted line. Shaded regions resemble the acceleration regimes indicated in (a) for small displacement. Dashed lines with arrows guide the eye along decreasing density in simulations, empty dots represent two selected experimental results with proton spectra shown in Fig. 3.

to  $r_c/r_0 \approx 3$  yields an estimate for the electron density at the interaction of approximately  $7n_c$ . A limitation of using the ordering parameter  $r_c/r_0$  to analyze the data is that the ordering parameter only corresponds to well-defined expansion under the assumption that the laser is centered on the sphere during the interaction. The jitter between laser and sphere also results in high probability of off-center interactions, which result in a higher transmission for given actual level of expansion and, therefore, slightly *lower* values of  $r_c/r_0$  when compared to a centered shot. Nonetheless, this proves a useful approach to analyzing the data in the following. Note that very low densities of a few  $n_c$  can also result in small values of the ordering parameter (see Appendix for a full discussion).

## III. RESULTS AND DISCUSSION

Figure 2(b) shows the maximum proton energy that can be achieved for each value of the ordering parameter. A rise in the highest energy can be seen at  $r_c/r_0 > 2$ , when compared to expanded targets  $r_c/r_0 < 2$ , where maximum proton energies never exceeded 20 MeV. The highest energies of up to 27 MeV are only observed for values of  $r_c/r_0$  in the range of 2.5–3.5. Best performance is, therefore, observed when the levitated spheres have a density that is approaching relativistically near-critical density, which will inform our numerical analysis of the experiment below.

Three-dimensional particle in cell simulations performed with the SMILEY code [31] aid the interpretation of the results (see Appendix for more information). The plasma was modeled as an equipartitioned mixture of protons and fully ionized carbon ions derived from polystyrene spheres ( $C_8H_8$ ) with an initial radius of 0.5  $\mu$ m. For unexpanded spheres, the

density distribution was constant with a radius of 0.5 µm. Radially symmetric Gaussian density distributions that contained the same number of particles as the initial sphere represented the pre-expanded spherical plasmas. Therefore, each simulation case could be associated to a critical density radius  $r_c$  and a central maximum electron density  $n_0$ at the start of the simulation. The differential proton energy distributions were extracted from the simulation in a plane 15 µm downstream of the initial sphere center. The simulations show a transition from a target normal sheath acceleration (TNSA)-type spherical expansion at high densities to a peak in achievable proton energies just before the plasma enters the regime of relativistic transparency, as shown in Fig. 2(a). We identify three regimes—TNSA, enhanced TNSA, and relativistic transparency—which are each highlighted with different colors. As the plasma density was not directly measured on each shot, the simulation results are also shown vs the ordering parameter in Fig. 2(b), which acts as a proxy for the target density. The maximum simulation proton energies are superimposed to the experimental results in Fig. 2(b) for the nonexpanded case  $n_0 = 195 n_c$  and nine pre-expanded cases with  $n_0 = 5, 7, 10, 15, 20,$  and  $50 n_c$ . The dashed lines in Fig. 2(b) connect the simulation results in the order of increasing expansion.

The simulation results match the experimental results well. The best shots for unexpanded spheres at  $195\,n_c$  match the simulation results as do the best shots at near critical density of around  $10n_c$ . The drop in maximum kinetic energy towards  $50\,n_c$  in the simulations is due to the reduction in peak kinetic energy for TNSA-dominated acceleration with increasing density scalelength at the boundary [32]. Compared to the simulations, the experimental data rises at

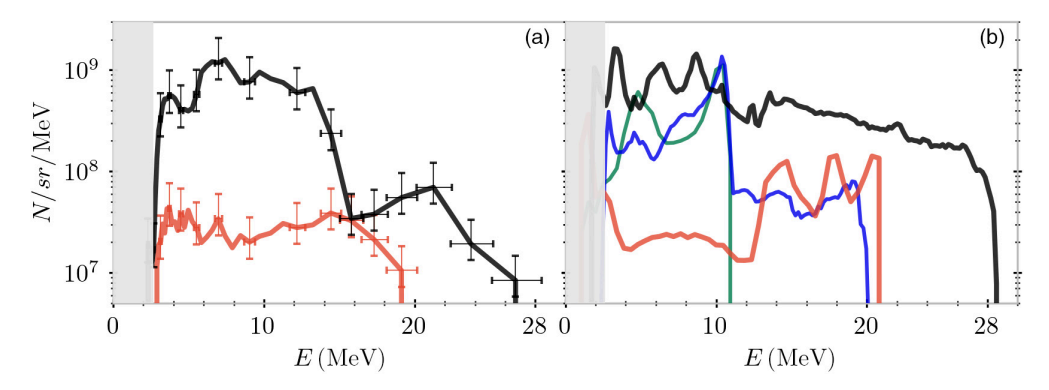


FIG. 3. Proton energy spectra. (a) Proton energy distributions (experiments) for centrally hit, non-pre-expanded sphere (red) and ideally pre-expanded sphere (black). Corresponding maximum energies are marked by empty dots in Fig. 2. (b) Proton energy distributions for simulations with nonexpanded sphere ( $n_0 = 195n_c$ , red), and expanded spheres with  $n_0 = 5$ , 7 and  $10n_c$  (green, blue, black).

somewhat-lower values of the ordering parameter in peak proton energies around  $r_c/r_0=2-2.5$ . This offset can be explained by spheres, which are expanded to optimum density  $(10-20~\rm n_c)$  but which have their ordering parameter reduced by misalignment between the sphere and the laser, as described above. To highlight the effect misalignment has, a dotted line shows how the point at  $20~\rm n_c$  shifts with increasing misalignment of the main beam relative to the target. The shaded areas show the expected shift resulting from a misalignment of up to 1  $\mu$ m from the adjacent simulation line. As can be seen, the overall effect of misalignment is not only to shift data-points to the lower values of  $r_c/r_0$ , but also to lower values of maximum energy in Fig. 2(b), due to the reduced coupling of laser energy to the target.

When relativistic transparency is reached around 7 n<sub>c</sub>, a sharp drop is seen for our parameter regime. This is due to the reduced laser coupling to the micro-plasma target. We note that extended near-critical targets have very different dynamics that do not apply here. The angular flux of the highest energy shots exceeds the peak flux for a spherical expansion by up to an order of magnitude, indicating strong beaming. In contrast, shots corresponding to low ordering parameters have a low angular proton flux (see Appendix for discussion). Figure 3(b) shows proton spectra extracted from the simulations for nonexpanded spheres  $(n_0 = 195 n_c)$ , as well as  $n_0 = 5, 7$ , and 10  $n_c$ . There is reasonable agreement with the experimental spectra in Fig. 3(a). The spectra in Fig. 3(a) correspond to the highest energies for a given ordering parameter and, hence, are presumed to have been hit centrally by the laser.

In the following discussion, we concentrate on the analysis of the  $10 \text{ n}_c$  case, as this yields the best results. Figure 4 shows details of the 3D PIC simulation with  $10n_c$  for our experimental parameters. We show snapshots of physical quantities at distinct times 14 and 2 fs (before the pulse peak arrives in the target center) and 14, 64, and 116 fs (thereafter). In detail, the following picture appears. During the laser-plasma interaction, the laser pulse interacts with an increasing electron density along the axis of its direction of propagation. Figure 4(a)—reveals that the laser pulse wraps around the plasma and accumulates electrons via its ponderomotive force, which acts both in propagation direction and radially towards the central axis. This creates a dense electron cloud that blocks the

laser and prevents the central part of the laser pulse from propagating on axis—causing the obscuration on our scatter screen experimentally. Because the electron density drops radially, the intensity of the outer part of the laser pulse passing the plasma remains high and this confines the electron cloud also radially during the time while the intensity of the pulse rises. This then allows the electrons to drag a substantial portion of both protons and carbon ions along via the strong longitudinal electric field [Fig. 4(b)] so that they form a thin and dense layer at the peak of the laser pulse [Figs. 4(c) and 4(d)]. This concerted motion of the laser reflection front and plasma density spikes continues for approximately the duration of the pulse and finally results in a collective motion of the target core in the direction of laser propagation. This is evident from comparing the density distributions with the initial target positions marked by the dotted circles, as well as in the longitudinal proton phase space in Fig. 4(e). We have extracted the position of maximum proton and carbon density that is visible in Figs. 4(c) and 4(d) as a function of time. The slope of the trajectories of these density peaks is nearly constant up to the peak of the pulse at 0 fs and reveals a velocity  $v_b$  of 9% of the speed of light c. The dense plasma layer is formed for all simulations with an initial density  $n_0 > 10n_c$  and its velocity scales as  $v_b \propto n_0^{-1/2}$ . This implies that the electrostatic force of the ions with mass  $m_i$  and the ponderomotive force of the laser with intensity  $I_L$  that both act on the electrons result in the momentum balance  $I_L/c = n_0 m_i v_b^2$  [5]. For our parameters, this yields  $v_b = 0.07 c$ . For  $n_0 < 10n_c$ , the laser penetrates the target and no high-density spike is formed. The factor 10 is close to the normalized vector potential amplitude of the laser pulse  $a_L$  and in line with the condition that the dense ion layer forms for electron densities larger than the relativistic critical density,  $n_0 \gtrsim a_L n_c$ . Although the velocity  $v \approx 0.09 c$ peaks for  $n_0 = 10n_c$ , this accounts only for a kinetic energy of 3.8 MeV. The most energetic protons, hence, must gain their velocity after the peak of the laser pulse has passed the plasma. The two late snapshots (62 fs and 116 fs) of proton density in Fig. 4(c) show that the fastest protons quickly gain an edge and outrun the moving plasma bunch.

Figure 4(e) shows the longitudinal phase space of protons at the respective times. During the interaction, protons from the target's laser-facing side are accelerated to positive (in the laser propagation direction) velocities up to  $0.1\ c$ . After the

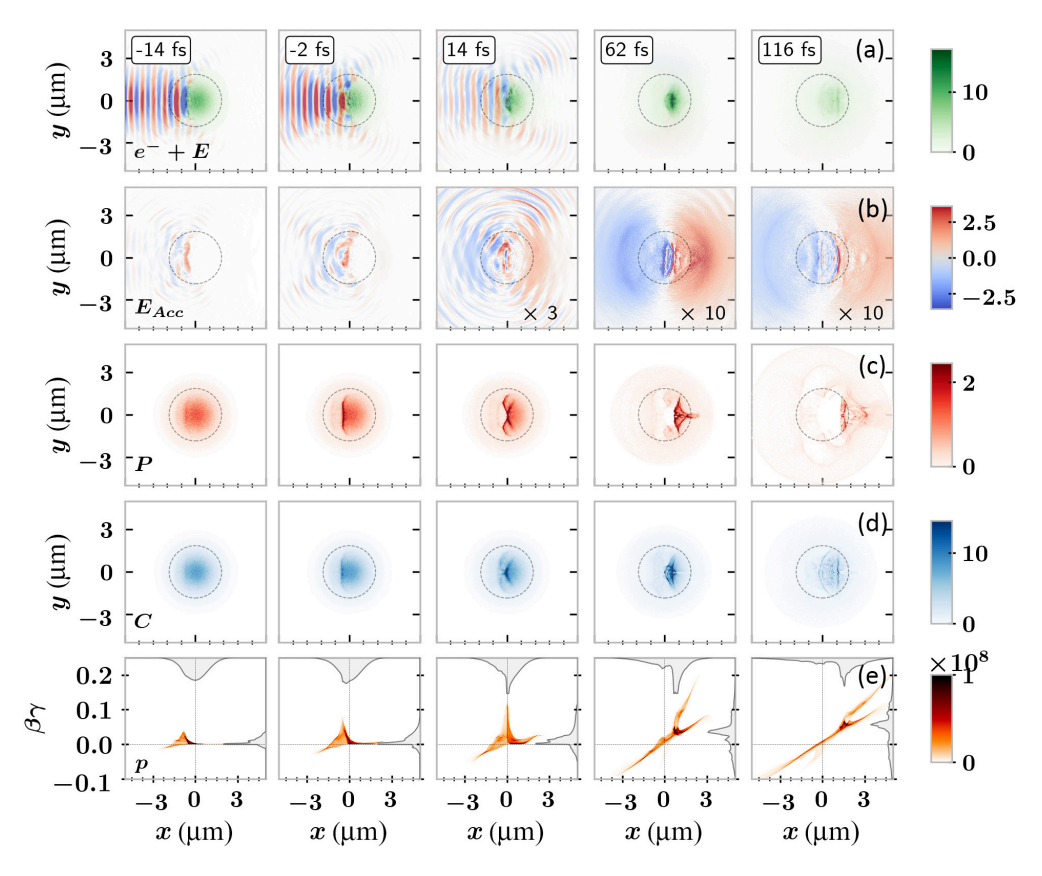


FIG. 4. PIC-simulation results for  $n_0 = 10n_c$ . (a) electron density (green colormap, in  $n_e/n_c$  and laser electric field [same colorbar as in (b)]. (b) Accelerating field along laser propagation direction in TV/m (blue-red colorscale). In the last three snapshots, the data is multiplied by a factor 3 and 10 for better visibility in the linear plots, (c) Proton density in  $n_p/n_c$ , (d) Carbon density in  $6n_C/n_c$ . (e) Distribution of protons in phase space along laser propagation direction and marginal of this distribution.

laser pulse has passed, the energy stored in the electric fields of the dense plasma bunch [Fig. 4(b)] is released, accelerating pre-accelerated protons from the target's front side, as well as protons from the target's rear side surface. The post-acceleration phase results in a cross-shaped pattern, with the steep arm of the distribution extending up to  $0.25\,c$ , equivalent to maximum kinetic proton energies of approximately  $30\,\mathrm{MeV}$  and close to our experimental observation.

This post-pulse phase of the acceleration is a consequence of the discharge of the field energy stored in the pre-accelerated plasma bunch. Consider that during the interaction of  $\tau_L \approx 22$  fs, a certain fraction of the laser pulse energy  $E_L$  is converted into electrostatic fields that drive the expansion. The accelerating field maps in Fig. 4(b) can yield the energy stored in this charge separation field by integration,  $\int \varepsilon_0 E_r^2 dx 2\pi r dr$ , and assuming cylindrical symmetry. We calculated the respective energy content in four different ways:  $r = y \ge 0$ ,  $r = y \le 0$ ,  $r = z \ge 0$ , and  $r = z \le 0$ . Because the electric field distribution is not strictly radially symmetric, this simple estimate provides bounds. The maximum appears at around 6 to 7 fs after the peak of the pulse and yields an energy between 13 and 34 mJ. This means between 3% and 9% of the laser energy are temporarily stored in the charge separation field. The maximum kinetic energy that a single proton can gain from this field is  $1 \text{ MeV} \cdot (\eta E_L/(\tau_L P_R))^{1/2}$ with the relativistic power unit  $P_R = 8.71 \,\text{GW}$  [33]. Using the values above, we calculate an energy in the range from 8 MeV

to 13 MeV, equivalent to an *excess* velocity between 0.13 c and 0.16 c. This agrees well with the excess longitudinal momentum observed in the steep arm of the phase space in the late snapshots in Fig. 4(e).

This is an astonishing result, considering that each of the two processes, hole-boring and expansion individually, support kinetic energies of 5 MeV (0.1 c) and 11 MeV (0.15 c), respectively. It is because the proton bunch expands while already moving with substantial velocity that fastest protons are accelerated to kinetic energies up to 30 MeV. We performed additional simulations for larger effective laser energies of 0.8, 4, and 8 J, where we kept all other initial parameters, in particular the initial sphere radius 0.5 µm constant, and varied only the initial central density  $n_0$  to meet the ideal acceleration conditions, see Fig. 5. As expected, the initial density required for maximizing the proton bunch energy increased with energy, though values between  $20 n_c$  and  $40 n_c$ yielded similar results. The maximum proton energy observed in the simulations scaled as  $E_m = k(E_L)^{1/2} = 54 \text{ MeVJ}^{1/2} \times$  $(E_L[J])^{1/2}$ , see inset in Fig. 5. This result agrees well with recent simulation studies by Matsui et al. that predicted proton energies between 200 and 300 MeV for laser pulse energies of up to 6 J in similar-sized, pure hydrogen clusters [34]. While the square-root scaling is in line with previous reports, the isolated micro-spheres are much more effective at achieving high ion energies with the factor k increasing  $\sim$  eightfold from 7.3 to 54 MeV/ $J^{1/2}$ .

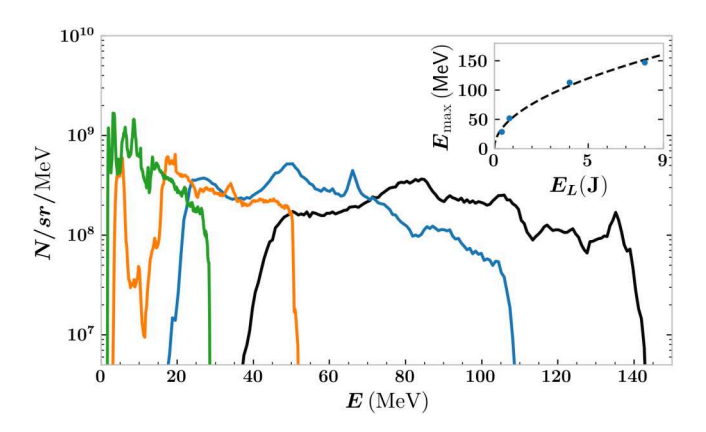


FIG. 5. Proton energy distributions from PIC simulations with laser pulse energy 0.4 J (green), 0.8 J (orange), 4 J (blue), and 8 J (black) and maximum energy as function of laser energy (inset) with square-root scaling (dashed).

#### IV. CONCLUSIONS

In summary, expanded micro-sphere targets were found to have more efficient conversion from laser energy in the central spot to maximum kinetic particle energy compared to thin foil experiments. This observation agrees well with the naïve expectation that mass-limited targets have less avenues for transporting energy away from the high intensity region and should, therefore, couple more effectively to the most energetic particles. The acceleration mechanism is a hybrid holeboring/sheath acceleration mechanism and reaches 28 MeV with an acceleration scaling parameter of 54 MeV/J<sup>1/2</sup>. This maximum kinetic energy per Joule laser energy is significantly higher than empirical results in planar targets. Pre-expanding the spheres to near-critical density is found to be essential for optimal coupling and acceleration as the lower density leads to an efficient bunch formation through radiation pressure with a subsequent acceleration due to sheath fields in the expansion phase. This high peak kinetic energy, therefore, results from the interplay of the fastelectron-driven expansion of a plasma bunch that is moving with significant fraction of the speed of light in the forward direction. Further optimization may be possible by shaping of the laser pulse [35] or optimizing the size of the isolated target. Nevertheless, according to our simulations, only 4 J of effective laser energy is predicted to be sufficient for achieving proton energies of 100 MeV. A state-of-the-art laser system with 10 J before the compressor would be able to provide the needed 4 J on target. Here we assumed a typical compressor transmission of 0.7, a plasma mirror reflectivity of 0.7 and a streel ratio of 0.8. This provides a first indication that accelerating protons to such energies and higher does not necessarily require PW lasers.

## **ACKNOWLEDGMENTS**

The authors thank G. Schäfer for operating the JETi200 laser system. This work was supported by the Helmholtz Institute Jena (HIJ), the Centre for Advanced Laser Applications (CALA), the Deutsche Forschungsgemeinschaft (DFG) under Grants No. 392856280 and No. 416702141 within the

Research Unit FOR2783. J.G. acknowledges support from the German Academic scholarship foundation.

#### DATA AVAILABILITY

The data are not publicly available. The data are available from the authors upon reasonable request.

#### **APPENDIX**

Laser. The experiments were conducted at the Jena-Ti:Sapphire (JETi200) CPA-Laser system at Helmholtz Institute Jena. A re-collimating plasma mirror enhanced the temporal contrast to  $10^8$  up to 5 ps before the peak of the pulse. After re-collimation, a 1-inch mirror picked a portion of the 12-cm-wide beam for generating the pre-pulse that could be timed via a delay stage between -1.8 ns and +200 ps relative to the main pulse arrival in focus. An iris reduced the pre-pulse diameter to approximately 6 mm before a second mirror positioned in the shadow of the first sent the pre-pulse back onto its initial path so that both main and pre-pulse were focused by the same off-axis parabolic mirror (OAP). The milled copper OAP had an off-axis angle of 90 degrees and an effective focal length of 18 cm, hence the f-number was 1.5 and 30 for main and pre-pulse, respectively. Due to losses in the compressor, the laser pulse delivery, the plasma mirror, and inherent pulse clips, the main pulse energy available for experiments was limited to 1.4 J, whereas the pre-pulse contained up to 0.8 mJ. Due to variations of the main beam profile from day to day, in particular in the outer region where the pre-pulse was picked, the resulting pre-pulse intensity varied between 10<sup>15</sup> and 10<sup>16</sup> W/cm<sup>2</sup>. This was found suitable for pre-expanding 1 µm polystyrene spheres to critical density within the available timing between pre- and main pulse. The focus of pre- and main pulse could be optimized separately and were overlapped using the focus diagnostics whenever the delay between pre-pulse and main pulse was changed. At the beginning of each experimental day, the focus shape was optimized by an adaptive mirror, yielding a spot with FWHM diameter of  $\approx$ 2  $\mu m$  FWHM diameter. The microstructure on the milled copper parabola created a lower intensity (>10<sup>15</sup> W/cm<sup>2</sup>) pedestal with a radial extent up to 50 µm. From this spatial energy distribution in focus, we estimate 20% of the laser energy to be contained within the FWHM diameter and this results in a peak intensity of  $\approx$ 6 × 10<sup>20</sup> W/cm<sup>2</sup>. As we have observed variations of the spot shape over longer times, we captured focal spot images every other hour during an experimental day.

Target. Our Paul-trap target system served for levitating polystyrene micro spheres (PS,  $C_8H_8$ ) with radius of (0.50  $\pm$  0.01) µm [microParticles Onlineshop, [36]]. Recent improvements on the system allowed automated target replacement, and an additional software interface enabled remote controlled operation so that, on average, one shot every 15 minutes could be performed. The sphere position was actively stabilized, the residual motion amplitude was <5 µm at residual gas pressures of <10<sup>-5</sup> mbar. Before each shot, the levitating sphere was imaged by the focal spot microscope and best possible overlap with the attenuated main pulse was ensured. Although time consuming, this procedure reduced uncertainties and also allowed recording the focal spot image close in time

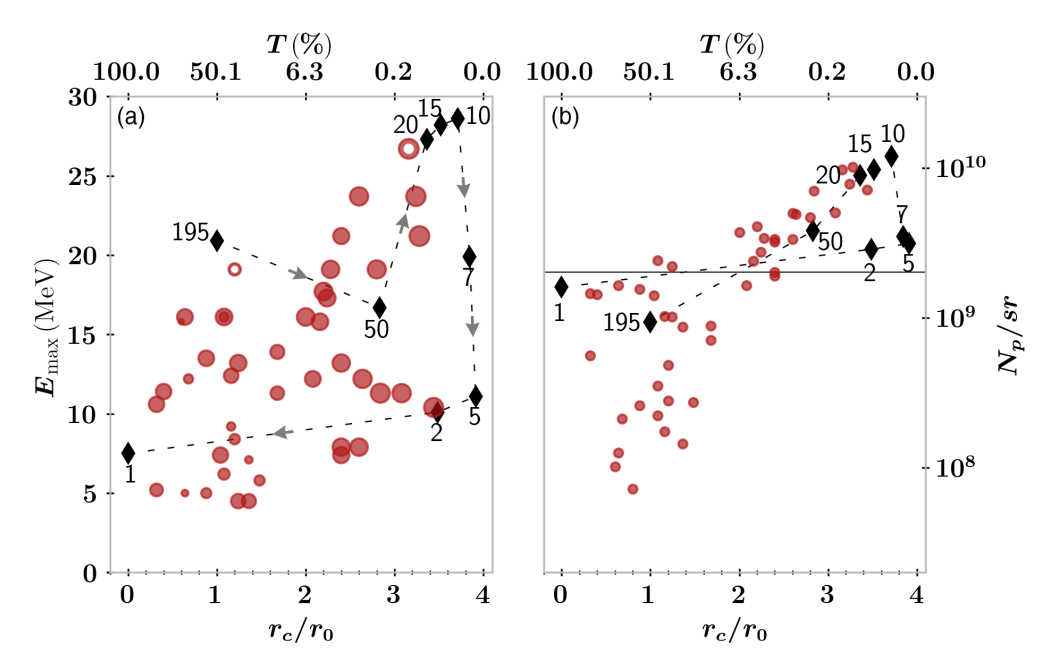


FIG. 6. (a) Same as plot 2(b) from main paper but with additional data that yielded lower proton energies and a line added between simulations at  $5n_c$  to  $1n_c$ . This line was omitted from the main section for clarity. It highlights the nonbijective relationship between the ordering parameter and peak density. Note that the ordering parameter is not defined for  $n_0 < n_c$ . The size of each data point encodes the angular flux. (b) Angular flux (above the detector threshold of 2.7 MeV) vs ordering parameter. The solid line is the calculated flux for a spherical expansion of our targets (assuming all particles above the detector energy threshold).

to the respective shot. When retracting the microscope to its parking position, the particle was monitored through a separate position monitor to ensure stable position until the laser shot. Larger diameter spheres were also shot, but resulted in lower proton energies.

Shot strategy. The experiments were conducted within several beamtimes and resulted in a total of 94 shots on 1  $\mu$ m spheres, of which 50 shots were hits in the sense that proton spectra could be retrieved. Due to changes in the laser profile over this long time, the picked pre-pulse energy varied by about one order of magnitude. The pre-pulse timing was actively chosen for each shot. The laser focal spot and particle position fluctuated, on average, within amplitudes of approximately 2  $\mu$ m, and this has remained the largest uncertainty in our experiments. We, therefore, decided to collect a large data set with sufficient variation to ensure that representative shots on spheres with all relevant pre-expansion parameters were covered.

Laser profile and  $r_c$ . A 500 mm x 500 mm anodized aluminum plate, 520 mm downstream of the target served as scatter screen for the laser profile after the interaction. The screen was imaged with a resolution of 0.25 mm. For each experimental day, one shot without target served as reference and for defining the illuminated area over which the signal was integrated. Integrating the laser profiles of shots with target over the same area and dividing by the reference shot value yielded the extinction by the target. This extinction was then predicted by assuming the plasma as a disc with radius  $r_c$  that blocks the central part of laser pulse with transverse Gaussian distribution and full width at half maximum (FWHM) diameter of 2  $\mu$ m. For the PIC simulations,  $r_c$  corresponds to the radius, where the simulated electron density distribution with peak density  $n_0$  has decayed to critical density  $n_c$ .

Particle spectrometer. The scatter screen had a slit with 1 mm height and 40 mm width that allows particles emitted from the plasma in a horizontal cone with  $\pm 2^{\circ}$  to pass and enter the particle spectrometer, composed of two sections. For both sections, the magnetic field was provided by permanent magnets shortened by iron yokes. The gap was 14 cm and the magnetic field in the center was approximately 0.1 T. The first dipole had a length of 24 cm followed by a drift of 44.5 cm, the second dipole had a length of 10 cm. After another drift of 29 cm, the dispersed ion cone beam created a two-dimensional ion dose map on a Fuji Film image plate detector (BAS-TR). The image plate was wrapped in 65 µm aluminum. Since the spectrometer did not use an electric field, there could be ambiguity on the detector since different ion species (e.g., H and C<sup>6+</sup>) could reach the same spot. To mitigate this problem, we covered different parts of the detector with aluminum slabs of increasing thickness. The different stopping powers for hydrogen and carbion ions allow us to identify certain areas on the detector, where the dose signal is solemnly caused by protons (under the assumption of an angular homogeneous beam). With this method we are able to reconstruct a proton spectrum with high signal to nose ratio due to the larger possible slit sizes. By this method spectra of carbon data con not be obtained. Due to cut off lines of carbons some estimates on carbon energy can be obtained.

The aluminum cover resulted in a minimum-detectable particle energy of 2.6 MeV for protons and 4.7 MeV/u for carbons. The energy-dependent penetration depth in aluminum was used to calibrate the vertical proton deflection to the particle energy. The image plate was large enough for accommodating up to four laser shots on fresh areas before replacement. The nonirradiated areas were shielded by 15-mm-thick aluminum plates. After four shots, the detector

was extracted and read out by an Amersham Typhoon scanner. The proton spectrum was acquired approximately on the central axis over an angle of 0.1° and in the region covered with only the 65 µm thick aluminum, enabling extraction of the widest-possible energy range of protons and ions. The background and noise level were estimated separately for each shot in nonirradiated regions and subtracted from the raw signal, before converting the signal to particle numbers via the image plate and scanner specific calibration factors. We employed the factory conversion to convert the signal from Raw data to PSL. Thereafter, we used an in-house calibration by cross referencing with another imageplate scanner via a beta-source to convert PSL to dose/proton numbers. The other image plate scanner was absolutely calibrated at a tandem accelerator [37].

Ordering parameter and peak density. The ordering parameter  $r_c/r_0$  is connected to density by the spherical expansion of the target to encompass a larger volume. However, the relation is not bijective. For our initial density and sphere size,  $r_c/r_0$  increases monotonically with decreasing peak density to  $n_0 = 5n_c$ . For lower peak densities, the  $r_c/r_0$  decreases again as the lower peak density of the Gaussian distribution results in a reduced radius  $r_c$  for which the density is still above  $n_c$ . As peak density reduces further  $n_0 \to n_c$ , the ordering parameter  $r_c/r_0 \rightarrow 0$ , since only a single point reaches the critical density. For peak densities  $n_0 < n_c$ , the ordering parameter is obviously not defined. Figure 6(a) shows the same data as Fig. 2 in the main section, but now including data with lower proton energies, as well, and with a line connecting the points  $5n_c$  to  $1n_c$  simulations. Strongly expanded spheres are, therefore, expected to sit at low ordering parameter and low peak proton energy.

Proton flux and ordering parameter. Further insight can be gained by considering the proton flux. Since the total number of protons is limited by size and composition of the sphere, we can easily calculate the expected flux for spherical expansion (TNSA-like). Figure 6(b) shows the dependence on ordering parameter for protons above the minimum detectable energy of 2.7 MeV. For unexpanded spheres the observed proton flux is close to, but just below the spherical expansion value. This is expected as there is a population of protons in TNSA-type acceleration with very low energies, which are not detected.

From the simulations shown in Fig. 4, one can see beaming of the accelerated protons, redistributing protons towards the detector. This is expected to increase the angular flux above values for a spherically symmetric expansion. This is, indeed, observed. Also, note that some very low ordering parameter shots exhibit beaming. These may correspond to overexpanded spheres, but are not clearly distinguishable from shots with lower expansion and significant pointing jitter.

PIC simulations. PIC simulations where performed with the SMILEI code. The 3D domain spanned  $40 \times 20 \times 20 \,\mu\text{m}^3$ with  $1600 \times 800 \times 800$  cells, equivalent to a spatial resolution of 25 nm and temporal resolution of 42 as. Boundaries were open for particles and absorbing for electromagnetic fields. The laser propagates along the positive x direction and is linearly polarized along the y axis. The laser pulse had a Gaussian intensity profile in focus with  $d_{\text{FWHM}} = 1.8 \, \mu\text{m}$ and duration  $\tau_{\text{FWHM}} = 32 \text{ fs}$ , as well as peak intensity of the experiment, which is a normalized vector potential amplitude of  $a_0 = 12$ , such that the contained energy was 0.4 J. For simulations with larger laser energy,  $a_0$  was scaled accordingly. The focus was positioned 10 µm from the left boundary and central in the remaining two spacial dimensions and its peak reaches this position after 5100 simulation steps and we refer to this time as t = 0. The initial plasma parameters are derived from a polystyrene sphere (C8H8) with a radius  $r_0 = 0.5 \,\mu\text{m}$ . We assume full ionization and this defines the electron density to  $n_e = 3.4 \times 10^{23} / \text{cm}^3 = 195 \,\text{n}_c$ . The initial temperature of the electrons was set to 2 keV.

In the nonexpanded case, each particle species (electrons, protons, carbon 6+ ions) was represented by 965 macro particles per cell and a constant density of 195 n<sub>c</sub> within the radius  $r < r_0 = 0.5 \,\mu\text{m}$  and zero outside. The pre-expanded cases were modeled with a truncated spherically symmetric Gaussian profile;  $n_e = n_0 \exp(-r^2/\sigma_r^2)$  for  $r < 6\sigma_r$  and zero for larger radii. We fixed the number of particles contained in the spherical plasma, therefore, the relation between maximum central densities  $n_0$  and plasma size  $\sigma_r$  is bound to  $n_0(\sigma_r/r_0)^3 = 4/(3\pi^{1/2}) \cdot 195$ . We recorded the momenta of protons and carbon ions when passing a plane 15 µm downstream of the target and generated the time-integrated energy distribution within a cone <0.1 rad in the forward direction for extracting maximum proton energy and angular particle fluence. In addition, we saved snapshots of relevant distribution functions every 75 simulation steps (3.2 fs) during the main interaction. After 6500 steps (60 fs after peak interaction), we reduced the temporal resolution to 300 steps (12 fs). The snapshots contain data of the electric and magnetic fields, as well as electron, proton, and carbon density and phase space distributions in the central polarization plane (x-y) and the perpendicular plane (x-z). For comparison to experimental results, we performed one simulation with the nonexpanded sphere ( $n_0 = 195n_c$ ) and nine simulations for increasingly expanded spheres with  $n_0 = 50, 20, 15, 10, 7, 5, 2$ , and  $1n_c$ . For exploration studies of increased laser energy, simulations were performed for  $n_0 = 10, 20, 28, 35$  with a laser energy of 4 J and  $n_0 = 10, 20, 30, 39$  for a laser energy of 8 J.

<sup>[1]</sup> R. A. Snavely et al., Phys. Rev. Lett. 85, 2945 (2000).

<sup>[2]</sup> T. Ziegler et al., Nat. Phys. 20, 1211 (2024).

<sup>[3]</sup> A. Macchi, M. Borghesi, and M. Passoni, Rev. Mod. Phys. 85, 751 (2013).

<sup>[4]</sup> S. C. Wilks et al., Phys. Plasmas 8, 542 (2001).

<sup>[5]</sup> S. C. Wilks, W. L. Kruer, M. Tabak, and A. B. Langdon, Phys. Rev. Lett. 69, 1383 (1992).

<sup>[6]</sup> T. Nakamura, S. V. Bulanov, T. Esirkepov, and M. Kando, Phys. Rev. Lett. 105, 135002 (2010).

<sup>[7]</sup> N. P. Dover et al., Light Sci. Appl. 12, 71 (2023).

<sup>[8]</sup> A. Henig et al., Phys. Rev. Lett. 103, 045002 (2009).

<sup>[9]</sup> D. Jung et al., Phys. Plasmas 20, 083103 (2013).

<sup>[10]</sup> L. Yin, B. J. Albright, B. M. Hegelich, and J. C. Fernández, Laser Part. Beams **24**, 291 (2006).

- [11] K. Nishihara, H. Amitani, M. Murakami, S. V. Bulanov, and T. Z. Esirkepov, Nucl. Instr. Meth. Phys. Res., Sect. A. 464, 98 (2001).
- [12] A. Robinson, P. Gibbon, M. Zepf, S. Kar, R. Evans, and C. Bellei, Plasma Phys. Control. Fusion 51, 024004 (2009).
- [13] T. Schlegel, N. Naumova, V. T. Tikhonchuk, C. Labaune, I. V. Sokolov, and G. Mourou, Phys. Plasmas 16, 083103 (2009).
- [14] L. O. Silva, M. Marti, J. R. Davies, R. A. Fonseca, C. Ren, F. S. Tsung, and W. B. Mori, Phys. Rev. Lett. 92, 015002 (2004).
- [15] A. Henig et al., Phys. Rev. Lett. 102, 095002 (2009).
- [16] T. Esirkepov, M. Borghesi, S. V. Bulanov, G. Mourou, and T. Tajima, Phys. Rev. Lett. 92, 175003 (2004).
- [17] A. Macchi, F. Cattani, T. V. Liseykina, and F. Cornolti, Phys. Rev. Lett. 94, 165003 (2005).
- [18] A. Henig et al., Phys. Rev. Lett. 103, 245003 (2009).
- [19] A. Macchi, S. Veghini, and F. Pegoraro, Phys. Rev. Lett. 103, 085003 (2009).
- [20] B. Qiao, M. Zepf, M. Borghesi, B. Dromey, M. Geissler, A. Karmakar, and P. Gibbon, Phys. Rev. Lett. 105, 155002 (2010).
- [21] J. Schreiber, F. Bell, and Z. Najmudin, High Power Laser Sci. Eng. 2, e41 (2014).
- [22] P. R. Bolton, K. Parodi, and J. Schreiber, Applications of Laser-Driven Particle Acceleration (CRC Press, Taylor & Francis Group, Boca Raton; London; New York, 2018).

- [23] M. Zimmer, S. Scheuren, T. Ebert, G. Schaumann, B. Schmitz, J. Hornung, V. Bagnoud, C. Rödel, and M. Roth, Phys. Rev. E 104, 045210 (2021).
- [24] W. Yu, H. Xu, F. He, M. Y. Yu, S. Ishiguro, J. Zhang, and A. Y. Wong, Phys. Rev. E 72, 046401 (2005).
- [25] Y. Fukuda et al., Phys. Rev. Lett. 103, 165002 (2009).
- [26] A. Stockem Novo, M. C. Kaluza, R. A. Fonseca, and L. O. Silva, Sci. Rep. 6, 29402 (2016).
- [27] A. Bhagawati and N. Das, Phys. Plasmas 29, 053107 (2022).
- [28] T. M. Ostermayr et al., Rev. Sci. Instrum. 89, 013302 (2018).
- [29] T. Ostermayr, Relativistically intense laser-microplasma interactions, Ph.D. thesis, LMU München: Fakultät für Physik, 2018
- [30] P. Hilz et al., Nat. Commun. 9, 423 (2018).
- [31] J. Derouillat *et al.*, Comput. Phys. Commun. **222**, 351 (2018).
- [32] A. J. Mackinnon et al., Phys. Rev. Lett. 86, 1769 (2001).
- [33] J. Schreiber et al., Phys. Rev. Lett. 97, 045005 (2006).
- [34] R. Matsui, Y. Fukuda, and Y. Kishimoto, Phys. Rev. Lett. 122, 014804 (2019).
- [35] T. Ziegler et al., Sci. Rep. 11, 7338 (2021).
- [36] https://www.microparticles-shop.de/.
- [37] S. Reinhardt, Detection of laser–accelerated protons, Ph.D. thesis, LMU München: Fakultät für Physik, 2012.